

Search for Axion-Like Particles from Nearby Pre-Supernova Stars

Saurabh Mittal¹, Thomas Siebert¹, Francesca Calore², Pierluca Carenza³, Laura Eisenberger¹, Maurizio Giannotti^{4,5},
Alessandro Lella^{6,7}, Alessandro Mirizzi^{6,7}, Dimitris Tsatsis¹, and Hiroki Yoneda^{1,8,9,10,11}

¹ Julius-Maximilians-Universität Würzburg, Fakultät für Physik und Astronomie, Institut für Theoretische Physik und Astrophysik, Lehrstuhl für Astronomie, Emil-Fischer-Str. 31, D-97074 Würzburg, Germany
e-mail: saurabh.mittal@uni-wuerzburg.de

² LAPTh, CNRS, USMB, F-74940 Annecy, France

³ The Oskar Klein Centre, Department of Physics, Stockholm University, Stockholm 106 91, Sweden

⁴ Centro de Astropartículas y Física de Altas Energías (CAPA), Universidad de Zaragoza, Zaragoza, 50009, Spain

⁵ Physical Sciences, Barry University, 11300 NE 2nd Ave., Miami Shores, Florida 33161, USA

⁶ Istituto Nazionale di Fisica Nucleare—Sezione di Bari, Via Orabona 4, 70126 Bari, Italy

⁷ Dipartimento Interuniversitario di Fisica Michelangelo Merlin, Via Amendola 173, 70126 Bari, Italy

⁸ The Hakubi Center for Advanced Research, Kyoto University, Yoshida Ushinomiya-cho, Sakyo-ku, Kyoto 606-8501, Japan

⁹ Department of Physics, Kyoto University, Kitashirakawa Oiwake-cho, Sakyo-ku, Kyoto 606-8502, Japan

¹⁰ RIKEN Nishina Center, 2-1 Hirosawa, Wako, Saitama 351-0198, Japan

¹¹ Kavli Institute for the Physics and Mathematics of the Universe (WPI), UTIAS, The University of Tokyo, 5-1-5 Kashiwanoha, Kashiwa, Chiba 277-8583, Japan

Received XXX; accepted YYY

ABSTRACT

Context. Axion-like particles (ALPs) are hypothetical pseudoscalar bosons that arise in many extensions of the Standard Model and can be well-motivated dark matter candidates. Nearby massive stars in the late stages of stellar evolution provide a promising environment for enhanced ALP production due to their high core temperatures and densities.

Aims. In this work, we search for a combined signal of ALP-induced hard X-ray and soft γ -ray emission from 18 nearby pre-supernova stars. We use the full public INTEGRAL/SPI 22-year database to create individual datasets and link the resulting spectra for a coherent analysis.

Methods. We use a maximum likelihood approach to extract the fluxes of the selected nearby stars from 20–2000 keV. From stellar evolution models, we obtain the expected spectral shapes of ALPs producing processes peaking in the range between 50–500 keV, depending on the age and mass of the star. We then construct a joint likelihood that acknowledges the uncertainties in individual stellar parameters towards a combined estimate for the coupling constants $g_{a\gamma}$ and g_{ae} as a function of the ALP mass m_a .

Results. We find that the hard X-ray and soft γ -ray fluxes of all selected stars are consistent with zero within uncertainties. We provide upper limits on the continuum flux as well as the 511 keV and 1809 keV lines from these sources. The combined estimate on the upper limit of the product $g_{a\gamma} \times g_{ae}$ is $(0.008 - 2) \times 10^{-24} \text{ GeV}^{-1}$ (95% C.I.) and the ALP-photon coupling $g_{a\gamma} = (0.13 - 1.26) \times 10^{-11} \text{ GeV}^{-1}$ (95% C.I.) up to a mass of $m_a \leq 10^{-11} \text{ eV}$ for different times to core-collapse and different magnetic field models.

Conclusions. Our results are among the strongest limits on the ALP coupling constants in the literature. We also provide conservative limits on the coupling constants $g_{a\gamma} \times g_{ae}$ of $(0.27 - 1.25) \times 10^{-24} \text{ GeV}^{-1}$ (95% C.I.) by assuming all stars but one to be in the early He burning phase. This work shows that soft γ -ray observations are required to efficiently probe the ALP parameter space, as well as massive star evolution models in general.

Key words. Stars: AGB and post-AGB – Stars: massive – Gamma rays: stars – Axion-like particles

1. Introduction

Axion-like particles (ALPs), including the special case of QCD axions, are hypothetical light pseudo-scalar particles that couple very weakly to photons and other standard model particles. Their interactions are described by the Lagrangian:

$$\mathcal{L}_{\text{int}} = -\frac{1}{4}g_{a\gamma}aF_{\mu\nu}\tilde{F}^{\mu\nu} - \sum_{f=e,p,n} g_{af}a\bar{f}\gamma_5f, \quad (1)$$

where $F_{\mu\nu}$ is the electromagnetic field strength tensor, $\tilde{F}^{\mu\nu}$ its dual, a the ALP field, and f the SM fermion fields (in our cases, we will be interested only in electrons, e). The coupling constants $g_{a\gamma}$ and g_{af} quantify the interaction strengths.

QCD axions were originally introduced to resolve the strong CP problem in quantum chromodynamics and are character-

ized by a model-dependent relationship between their mass and coupling constants (Di Luzio et al. 2020). More general ALPs emerge in several extensions of the Standard Model (SM) of particle physics (Jaeckel & Ringwald 2010; Ringwald 2014; Agrawal et al. 2021; Giannotti 2023; Antel et al. 2023) and lack any specific relation among couplings and mass.

From a top-down perspective, string theory predicts the presence of an “axiverse” with the QCD axion (Peccei & Quinn 1977b,a; Weinberg 1978; Wilczek 1978) and several ultralight ALPs (Arvanitaki et al. 2010; Cicoli et al. 2012, 2024). From a bottom-up perspective, ALPs offer an interesting physics case in relation to dark matter (Abbott & Sikivie 1983; Dine & Fischler 1983; Preskill et al. 1983; Arias et al. 2012; Adams et al. 2022) and to several astrophysical puzzles (Giannotti et al. 2016, 2017; Galanti et al. 2023). In this context, stars have long been recog-

nized as ALP factories (Raffelt 1996, 1999; Carena et al. 2025), as stellar plasmas provide ideal conditions for producing large fluxes of these particles. The production of ALPs under these extreme temperature and density conditions, provides an additional channel for energy loss. This can alter the evolution of horizontal branch stars (Ayala et al. 2014; Straniero et al. 2015; Dolan et al. 2022), red giants (Capozzi & Raffelt 2020; Straniero et al. 2020), and white dwarfs (Bertolami et al. 2014). Moreover, ALPs have been proposed as a possible explanation for the so-called stellar cooling anomaly—the observed excess cooling in several classes of stars (Giannotti et al. 2017, 2016). Additionally, they can also be used as supernova (SN) probes since they are able to exit the stellar interiors earlier than photons (Lella et al. 2024). A comprehensive overview of the astrophysical implications of ALPs can be found in Carena et al. (2025).

Notably, just a few years after the introduction of the QCD axion, Pierre Sikivie (Sikivie 1983) proposed to search for this elusive particle through dedicated observations of the Sun via the “helioscopes” technique (van Bibber et al. 1989). The key idea of these types of experiments is that in the case of a ALP-photon coupling $g_{a\gamma}$, ALPs can be produced in the Sun’s core via Primakoff process (Carlson 1995; Primakoff 1951), and then convert into X-rays in the magnetic field of the detector (Andriamonje et al. 2007). The CAST experiment, the most mature example of axion helioscope (Cetin 2024), has recently presented a new analysis (Altenmüller et al. 2024), improving the previous bound from Solar ALPs down to $g_{a\gamma} < 5.7 \times 10^{-11} \text{ GeV}^{-1}$ for $m_a \lesssim 0.02 \text{ eV}$. The next generation of helioscopes, BabyI-AXO Abeln et al. (2021b); Ahyoune et al. (2025) and the full scale IAXO Armengaud et al. (2019); Arcusa et al. (2025), aim to improve the sensitivity to the axion–photon coupling relative to CAST by a factor of 3 and by more than an order of magnitude, respectively.

The Sun is the closest star to us, so one would expect it to be the best target for astrophysical ALPs searches. However, other stellar environments have been shown to have a competitive physics potential. Notably, after the SN1987A neutrino observations, the occurrence of ALP burst produced in the SN core, simultaneously with neutrinos, was searched for. Notably, SN ALPs would have led to a gamma-ray burst, induced as a consequence of ALP-photon conversions in the Galactic magnetic field. The non-observation of such a signal in the Gamma-Ray Spectrometer (GRS) of the SMM (Solar Maximum Mission) in coincidence the neutrino signal from SN 1987A, provided a strong bound on ALPs coupled to photons (Grifols et al. 1996; Brockway et al. 1996; Hoof & Schulz 2023). For $m_a < 4 \times 10^{-10} \text{ eV}$ it was found $g_{a\gamma} < 5.3 \times 10^{-12} \text{ GeV}^{-1}$ (Payez et al. 2015).

Other promising stellar sources for ALPs are nearby red supergiant (RSG) stars. Indeed, their high core temperatures and the steep dependence of the ALP production rate on temperature make them compelling sources of stellar ALPs. Remarkably, there are ~ 20 supergiants with masses ranging from $10 - 30 M_{\odot}$ within a distance $d \lesssim 1 \text{ kpc}$.

An example studied quantitatively is the red supergiant star Betelgeuse (α Orionis), spectral type M2Iab at a distance $d \simeq 197 \text{ pc}$ (Dolan et al. 2016), proposed as ALP target in a seminal paper by E. Carlson Carlson (1995). Recently, Xiao et al. (2021) used the data of a dedicated 50 ks observation by the NuSTAR satellite (Harrison et al. 2013) to place a 95% C.I. upper limit on the ALP-photon coupling $g_{a\gamma} < (0.5 - 1.8) \times 10^{-11} \text{ GeV}^{-1}$ for ALP masses $m_a < (5.5 - 3.5) \times 10^{-11} \text{ eV}$, assuming only Primakoff production. Enlarging the production channels to include,

besides the Primakoff process, also bremsstrahlung and Compton processes induced by the ALP-electron coupling g_{ae} , Xiao et al. (2022) derived the constraint $g_{a\gamma} \times g_{ae} < (0.4 - 2.8) \times 10^{-24} \text{ GeV}^{-1}$ for masses $m_a \leq (3.5 - 5.5) \times 10^{-11} \text{ eV}$. Fig. 1 shows the Feynman diagrams for the three ALP production mechanisms.

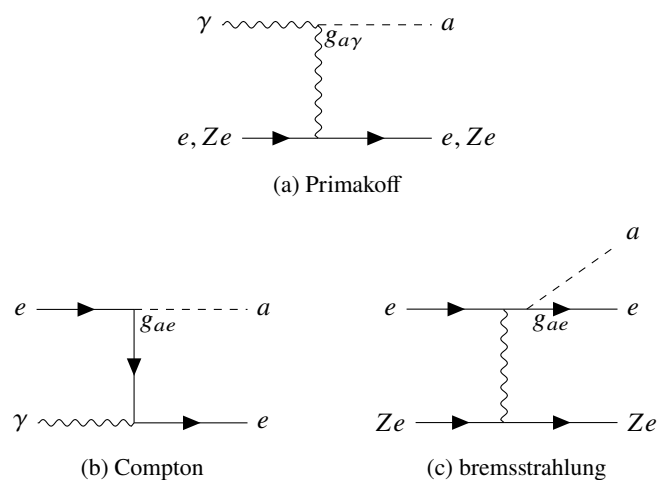


Fig. 1: Feynman diagrams for ALPs production: Primakoff, Compton, and bremsstrahlung.

The search we perform in this work is complementary to the study by Xiao et al. (2022). Here, we extend their efforts to the γ -ray regime ($20 - 2000 \text{ keV}$) for Betelgeuse and 17 additional nearby ($< 1 \text{ kpc}$) red super giants using data from INTEGRAL/SPI (Winkler et al. 2003; Vedrenne et al. 2003).

This paper is structured as follows: In Sec. 2, we describe our selection of candidate stars. Sec. 3 recapitulates on the expected spectral signatures from ALPs. Our data analysis method is described in Sec. 4. We present our results in Sec. 5 and conclude with an outlook in Sec. 6.

2. Source selection

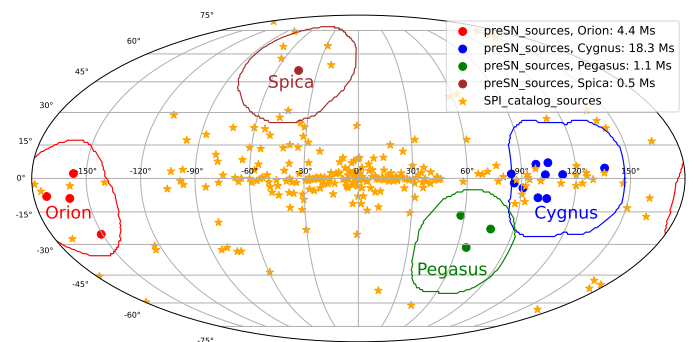


Fig. 2: The orange stars show the location of all the detected sources with SPI so far (Bouchet et al. 2008). The circular dots are the red super giants used in this work. The colored boundaries are the exposure regions for each dataset.

The star sample chosen is a subset of the catalog provided in Mukhopadhyay et al. (2020). The catalog originally lists 31 core-collapse SN progenitors within 1 kpc that have both distance and mass estimates. These massive stars are believed to be in the late stages of nuclear burning close to core-collapse. We shortlist 18

red super giant candidates from this list. In Tab. 1, we present the details of the selected sources including their Galactic coordinates, common names, mass and distance. The stars are selected in a way that they are at large enough distances from bright sources in the SPI catalog (no bright sources within a 30° radius of our candidate source) and from potentially variable sources to avoid systematics from source confusion and variability.

Our final star sample consists of Betelgeuse (in close proximity with the Crab nebula, the brightest γ -ray source seen by INTEGRAL, and partly in SPI's field-of-view), CE Tauri (also close to the Crab nebula and Betelgeuse), Rigel (Orion region), ten stars in the Cygnus region (carefully selected to avoid Cyg X-1), three stars in the Pegasus region, Spica, and S Monocerotis A (Orion region) (Fig. 2).

3. ALP spectrum and stellar models

The ALP source spectrum from a red super giant star can be approximated by

$$\begin{aligned} \frac{d\dot{N}_a}{dE} = \frac{10^{42}}{\text{keV s}} & \left[C^B g_{13}^2 \left(\frac{E}{E_0^B} \right)^{\beta^B} e^{-(\beta^B+1)E/E_0^B} \right. \\ & + C^C g_{13}^2 \left(\frac{E}{E_0^C} \right)^{\beta^C} e^{-(\beta^C+1)E/E_0^C} \\ & \left. + C^P g_{11}^2 \left(\frac{E}{E_0^P} \right)^{\beta^P} e^{-(\beta^P+1)E/E_0^P} \right], \end{aligned} \quad (2)$$

where $g_{11} = g_{a\gamma}/10^{-11} \text{ GeV}^{-1}$, $g_{13} = g_{ae}/10^{-13}$, $C^{B/C/P}$ are the normalizations, $E_0^{B/C/P}$ are the cut-off energies, and $\beta^{B/C/P}$ are the spectral indices for bremsstrahlung, Compton, and Primakoff processes, respectively. This follows the description of Xiao et al. (2022) which uses the Full Network Stellar evolution code (FuNS (Straniero et al. 2019)) to derive the fluxes and spectral shapes. The values for these parameters in the case of Betelgeuse had been obtained from previous simulations (Xiao et al. 2022) for different times to core-collapse (t_{cc}). The fluxes depend on the temperature and density conditions directly derived from the hydrodynamics profiles provided by the code. All the stellar models considered lead to a surface luminosity able to reproduce the position of these stars in the Hertzsprung-Russell diagram. The models cover a wide range of stellar evolutionary phases which reproduce the observational data. The closer a star is to core-collapse, the hotter is its core, and therefore should have a higher ALP production rate, resulting in a higher γ -ray flux. In Fig. 3, we show the expected ALP flux contributions from the three production mechanisms as well as their combined spectrum for Betelgeuse at a time to core-collapse of 6900 yr. For comparison, we indicate the energy upper limit of NuSTAR (79 keV; blue dashed line), highlighting that the bulk of the ALP-induced emission lies above NuSTAR's sensitivity and extends into the soft γ -ray regime. This emphasizes the suitability of using INTEGRAL/SPI, to probe this energy range.

The differential photon flux per unit energy arriving at Earth is

$$\frac{dN_\gamma}{dE dS dt} = \frac{1}{4\pi d^2} \frac{d\dot{N}_a}{dE} P_{a\gamma} \equiv F(E_{ini}, m_a, g_{a\gamma}, g_{ae}), \quad (3)$$

where $P_{a\gamma}$ is the ALP-photon conversion probability given by

$$P_{a\gamma} = 8.7 \times 10^{-6} g_{11}^2 \left(\frac{B_T}{1 \mu\text{G}} \right)^2 \left(\frac{d}{197 \text{ pc}} \right)^2 \frac{\sin^2(qd)}{(qd)^2}. \quad (4)$$

Here, B_T is the Galactic magnetic field, d is the distance to the star, and q is the momentum transfer (Xiao et al. 2022). The product of the momentum transfer q , and the distance d is given by

$$qd \simeq \left[77 \left(\frac{m_a}{10^{-10} \text{ eV}} \right)^2 - 0.14 \left(\frac{n_e}{0.013 \text{ cm}^{-3}} \right) \right] \times \left(\frac{d}{197 \text{ pc}} \right) \left(\frac{E}{1 \text{ keV}} \right)^{-1}. \quad (5)$$

Here, m_a is the mass of the ALP and n_e is the electron density. For sources within $< 1 \text{ kpc}$, we assume a uniform electron density ($n_e = 0.013 \text{ cm}^{-3}$) and three Galactic magnetic field scenarios with uniform Galactic magnetic field ($B_T = 0.4, 1.4, 3.0 \mu\text{G}$). These values are motivated by measurements of Betelgeuse as also quoted in (Xiao et al. 2022). Since the Galactic magnetic field at \sim hundred pc distances is not very well modeled, we use Betelgeuse as indicative, and using these three above mentioned B_T scenarios help us cover a wide range of realistic possibilities. The given spectrum and expected flux contributions are specifically created for Betelgeuse. However, we also use it for other stars even though the parameters might depend on the mass of the star. The mass distribution of our stellar sample ranges from $5 M_\odot - 29 M_\odot$ with the average mass of a star being $\sim 11.5 M_\odot$. The average star mass is comparable to Betelgeuse, and due to our combined analysis approach, it is a fair assumption to apply this same spectrum to other stars.

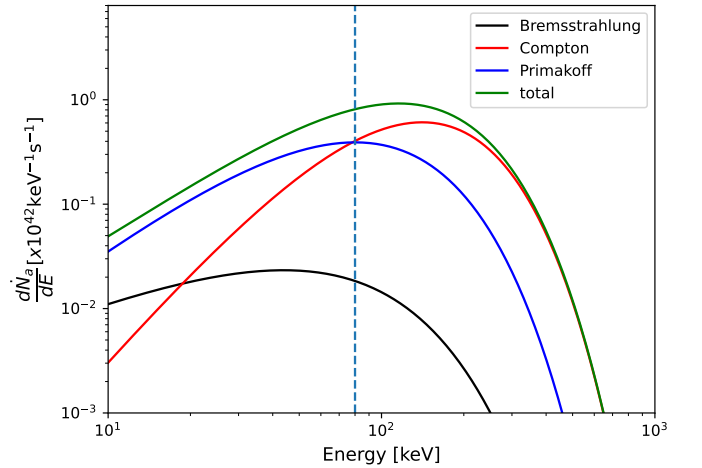


Fig. 3: Expected ALP fluxes from bremsstrahlung (black), Compton (red), Primakoff (blue), and total (green) using $g_{ae} = 10^{-13}$, $g_{a\gamma} = 10^{-11} \text{ GeV}^{-1}$, and a time to core-collapse of $t_{cc} = 6900 \text{ yr}$. The blue dashed line shows the energy upper limit of NuSTAR (79 keV).

4. Dataset and analysis

4.1. SPI data analysis

We use INTEGRAL/SPI observations in the energy range 20 – 2000 keV, with a field of view of 20° , around the regions of Orion/Betelgeuse (4.4 Ms, 1770 pointings, 2486 sec per pointing), Cygnus (18.3 Ms, 7463 pointings, 2452 sec per pointing), Pegasus (1.1 Ms, 482 pointings, 2282 sec per pointing), and Spica (0.5 Ms, 239 pointings, 2092 sec per pointing). We select pointings that fall within a 10° radius around our source of interest namely Betelgeuse ($l = 199.787^\circ$, $b = -8.959^\circ$), Rigel ($l = 209.24^\circ$, $b = -25.24^\circ$), Spica ($l = -43.88^\circ$, $b = 50.84^\circ$), Pegasus ($l = 76^\circ$, $b = -37^\circ$), and for Cygnus a rectangular region spanning

($l = [100^\circ, 130^\circ]$, $b = [-10^\circ, 10^\circ]$) (shown in Fig.2 with exposure outlines). Data from SPI are modeled in the following way:

$$d_{i,j,k} = \sum_l R_{l,ijk} \sum_{n=1}^{N_s} \alpha_{nk} S_{nl} + \sum_{n=N_s+1}^{N_s+N_b} \beta_{nk} B_{n,ijk}, \quad (6)$$

where, $d_{i,j,k}$ is the event counts with i, j, k being the indices of pointing, detector, and energy bin that spans the data space, respectively. $R_{l,ijk}$ is the instrument response for a given sky direction, l . This also includes the effective area and determines the point spread function. The energy dispersion is included in the spectral fit which are named as E_{ini} , E_{fin} . α_{nk} and β_{nk} are the normalization factors (model parameters) for the N_s sky model components, S_n , and N_b background model components, B_n , respectively (Diehl et al. 2018). We assume no a priori spectra, so the extracted data points for each source (flux values), correspond to α_{nk} for each of the n sources. The background is created from the SPI background and response data base (Diehl et al. 2018; Siebert et al. 2019). The background at a specific energy bin is modeled using two components: photons from continuum processes, and photons from γ -ray lines. For a specific physical process inside the satellite, the detector patterns from the background stay constant. The only thing that might change as a function of time/pointing is the amplitude of the two background components which is determined in a maximum likelihood fit. The sky model is defined by a list of already known SPI point sources (Bouchet et al. 2008) (Fig. 2 orange), the diffuse positron annihilation signal, and the diffuse 1.8 MeV line from the decay of ^{26}Al and any additional source one would like to fit. In the Betelgeuse dataset, this would mean 5 SPI point sources, plus our 4 red super giant candidates (Betelgeuse, Rigel, CE Tauri, and S Monocerotis A at their respective positions), plus the diffuse positron annihilation map (Siebert et al. 2016) for 467.5–514 keV, plus the diffuse ^{26}Al map for the 1809 keV bin. To account for any possible strong and/or variable source contamination such as from the Crab, narrow energy bins (0.5 keV bins from 20 – 105 keV, 2 keV bins from 105 – 203 keV, and logarithmic bins from 203 – 2000 keV) were used for the Betelgeuse region. Such narrow energy bins would result in oversampling the energy dispersion. The oversampling is only to account for the highly variable background (strong lines) and is not relevant here because the ALP model spectra are broadband. For the other three regions, logarithmic energy bins were found sufficient and narrow bins did not significantly affect the quality of the fit. Finally, we use OSA/spimodfit (Courvoisier et al. 2003; Strong et al. 2005) to extract the flux per energy bin by fitting the SPI data using Eq. (6).

After an initial maximum likelihood fit to extract the SPI spectrum from the raw detector counts by fitting the sky and background model components independently in each energy bin Eq. 6, we found that some of the observations (Betelgeuse region: 8%, Cygnus region: 3%) were contaminated by investigating the residuals as a function of pointing ID. We iteratively removed these “bad pointings” by clipping outliers which deviate from our expectation by more than 5σ . Such outliers typically originate in solar particle events or transients which are not modeled in this approach. This results in typical goodness-of-fit values of χ^2/dof of Orion: 1.02 ± 0.02 , Cygnus: 0.89 ± 0.02 , Pegasus: 0.99 ± 0.03 , Spica: 1.00 ± 0.02 , which is adequate given the number of data points in each dataset being around 33630, 141797, 9158, and 4541 respectively. We quote the mean and standard deviation of these per bin χ^2/dof values to demonstrate the quality of the background and sky modeling in each region. These values only serve as a diagnostic of SPI spectral extraction.

The γ -ray spectrum obtained from SPI for Betelgeuse in particular, and all other 17 sources as well, is consistent with zero, leading us to estimate upper limits for the two couplings. Fig. 4 shows the extracted SPI spectrum of Betelgeuse to which different ALP spectra (age: 1.55×10^5 –3.6 yr, Galactic magnetic field B_T : 0.4, 1.4, 3.0 μG , distance d : 222 pc, electron density n_e : 0.013 cm^{-3} , and ALP mass m_a : 10^{-14} – 10^{-9} eV) were fitted. The spectra are fitted with a Gaussian likelihood, corresponding to χ^2 ,

$$\chi^2(\alpha_k | M_k(m_a, g_{a\gamma}, g_{ae})) = \sum_k \left(\frac{\alpha_k - M_k(m_a, g_{a\gamma}, g_{ae})}{\sigma_{\alpha_k}} \right)^2 \quad (7)$$

with

$$M_k(m_a, g_{a\gamma}, g_{ae}) = \frac{1}{\Delta E_k} \int_{E_{min,k}}^{E_{max,k}} F(E_{ini}, m_a, g_{a\gamma}, g_{ae}) \cdot R(E_{ini}) dE_{ini}, \quad (8)$$

where α_k is the extracted flux values, σ_{α_k} are the uncertainty on the flux values, and R is the instrument response matrix. This χ^2 is the statistical quantity that is used to evaluate the ALP model parameters and is unrelated to the χ^2/dof values quoted for the SPI spectral extraction process. Since the spectrum is consistent with zero, we show the 3σ upper limits for energy bins where the flux significance is $< 2\sigma$. In the red shaded region, we also show the flux allowed by earlier constraints, such as from the NuSTAR study by Xiao et al. (2022), which is now disallowed in this study since the flux expectation is higher than the 3σ flux measured by SPI. Similarly, the blue shaded region are the allowed flux values that were already rejected in the NuSTAR study.

For the spectral analysis, we use 14 different ALP spectra combinations, 12 of which are for $B_T = 1.4 \mu\text{G}$ and t_{cc} ranging from 1.55×10^5 –3.6 yr (Xiao et al. 2022), one for $B_T = 3.0 \mu\text{G}$ and $t_{cc} = 3.6$ yr, and one for $B_T = 0.4 \mu\text{G}$ and $t_{cc} = 1.55 \times 10^5$ yr. Such a wide range of spectral model combinations ensure that the entire range of possibilities is accounted for, ranging from very conservative case (low Galactic magnetic field and early phases of stellar evolution) to most optimistic case (high Galactic magnetic field and late stages of stellar evolution). Therefore, any possible realistic scenario would always lie in the range of coupling constants obtained from these two extreme cases.

4.2. Hierarchical modelling approach

Fig.5 presents the Bayesian hierarchical model used to jointly constrain the properties of ALPs from γ -ray observations of the 18 sources. The three key ALP parameters, the ALP mass m_a , ALP-photon coupling $g_{a\gamma}$, and the ALP-electron coupling g_{ae} , are treated as global parameters, linked across all sources, and were assigned priors in a Bayesian inference framework. These govern both the production of ALPs in stellar interiors and their conversion to photons in the Galactic magnetic field.

To perform the combined analysis, we assume a shared spectral shape for the ALP induced γ -ray flux across all stars ($n = 1 \dots 18$) as the underlying physical mechanisms in all stars remain the same. This spectral shape is derived from standard ALP emission processes (Compton, Primakoff, bremsstrahlung) and depends on t_{cc} , $g_{a\gamma}$, g_{ae} . The ALP-photon conversion probability $P_{a\gamma}(m_a, g_{a\gamma}, B_T, n_e, d_n)$ further modifies this spectrum, depending on the fixed parameters $B_T = (0.4, 1.4, 3.0) \mu\text{G}$, $n_e = 0.013 \text{ cm}^{-3}$, and the distance to each star d_n , which may also be uncertain but our assumption of a uniform magnetic field helps us eliminate the distance dependence in the expected photon flux. While the spectral normalization varies from star to

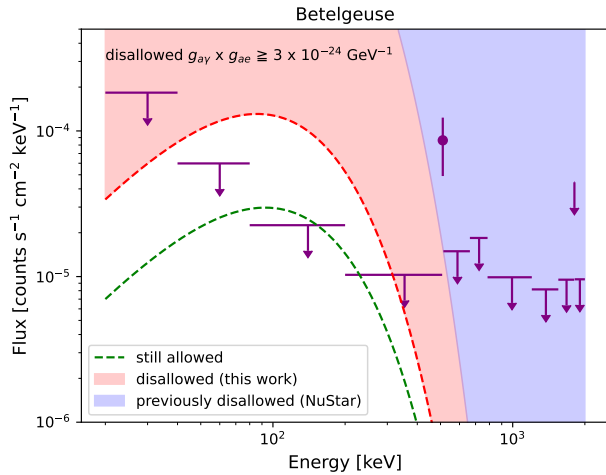


Fig. 4: Betelgeuse spectrum as obtained from SPI for the energy range 20 – 2000 keV. The dot with the error bar shows the flux value in that energy bin. The downward arrows show the 3σ upper limit for bins where the flux significance is less than 2σ . The 511 keV bin is systematically large because of incomplete modelling of the diffuse emission in the Crab/Orion region and is therefore not taken as a detection of 511 keV in Betelgeuse. The red shaded region shows the flux from the $g_{a\gamma} \times g_{ae}$ values allowed by NuSTAR that can now directly be excluded from the ALP parameter space since the flux prediction from them is larger than the 3σ flux limits from SPI. The excluded limit is $g_{a\gamma} \times g_{ae} \geq 3 \times 10^{-24} \text{ GeV}^{-1}$. The blue shaded region shows the flux from the $g_{a\gamma} \times g_{ae}$ values that were already disallowed in the NuSTAR study (Xiao et al. 2022).

star due to differences in d_n (scaling as $1/4\pi d_n^{-2}$), the underlying spectral shape and the governing ALP parameters are common to all sources. Each star’s predicted photon flux F_n is obtained by scaling the ALP luminosity, $L_n = d\dot{N}_a/dE \times P_{a\gamma}$ by the respective distance (see Eq. 3). The smooth astrophysical models in units of $\text{ph cm}^{-2} \text{ s}^{-1} \text{ keV}^{-1}$ are then converted to observable counts by applying the instrument response matrix $R(E_{\text{ini}}, E_{\text{fin}})$ (Eq. 8). An additional component $F_{\text{intrinsic},n}$ may account for known γ -ray line or continuum emissions, including the 511 keV positron annihilation line and positronium continuum, and the 1.809 MeV line from ^{26}Al decay unless modeled already in the spectral extraction step. The full model is fitted to the observed data α_{nk} for each star via a likelihood function (Eq. 7), and the fit is performed jointly across all 18 stars using the 3ML (Multi-Mission Maximum Likelihood) framework (Vianello et al. 2015). 3ML allows for shared parameters across multiple datasets, enabling a coherent global fit in which the particle physics parameters $m_a, g_{a\gamma}, g_{ae}$ are constrained simultaneously using all available information and uncertainties. The model thus fully exploits the consistency of ALP physics across stellar environments while accounting for differences in source distances, instrumental responses, and intrinsic background features.

5. Results

5.1. Individual Stars

We use a representative ALP spectrum (also taken from Xiao et al. 2022) to fit our source spectrum and estimate the param-

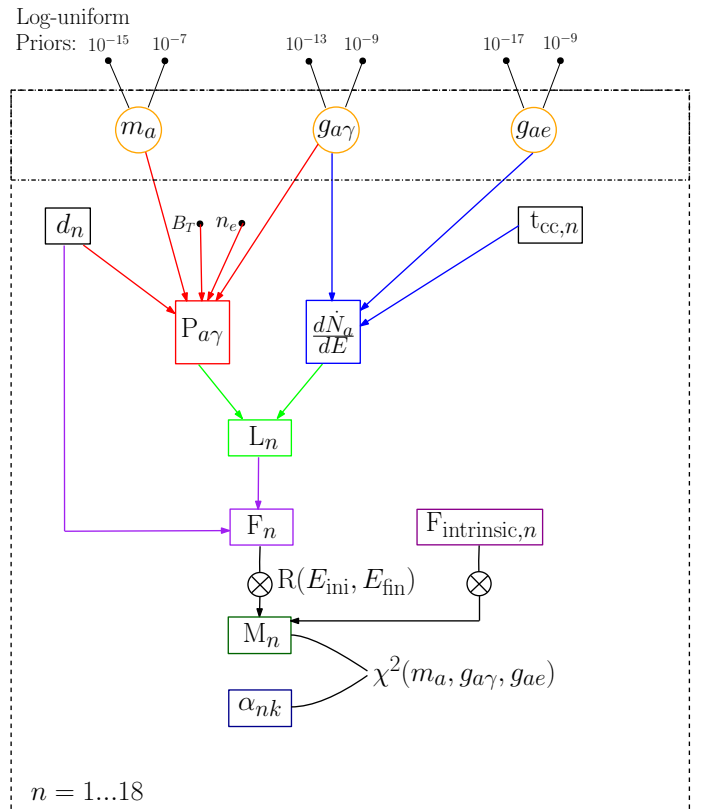


Fig. 5: Bayesian hierarchical model used to constrain the ALP parameters $m_a, g_{a\gamma}, g_{ae}$. The model assumes that these global parameters are shared across all 18 sources and govern both ALP production in stellar interiors and their conversion to photons in the Galactic magnetic field. Each star contributes a predicted photon flux based on its luminosity, distance, and a shared ALP spectral shape. This flux is convolved with the instrument response to yield the expected counts which are compared to the observed data. A joint likelihood analysis is performed across all sources using the 3ML framework to obtain constraints on the ALP parameter space.

eter values of $g_{ae} \times g_{a\gamma}$ for a given range of m_a . Fig. 6 shows the 95% C.I. obtained from Betelgeuse for our set of available stellar models. We find that the constraints obtained from SPI for Betelgeuse are a factor of ~ 5 better than those estimated from NuSTAR. This improvement is also shown in Fig. 6.

In Fig. 7, we show the 95% C.I. obtained for each individual star and from a combined analysis of all stars (see 4.2) for a representative stellar model $t_{\text{cc}} = 6900 \text{ yr}$ and $B_T = 1.4 \mu\text{G}$. We find that not all stars result in the same limits, as expected from the different exposure times and distances. We assume each star can be modeled by the spectrum estimated for Betelgeuse (Xiao et al. 2022). While the detailed spectral shape may vary with stellar mass, the underlying physical processes governing ALP production are expected to be similar for stars in comparable evolutionary stages. Additionally, we assume that all stars are in the same burning phase. These assumptions ensure that any realistic scenario would lie within the range spanned by the various combinations of this model, thereby providing a range of possible constraints. We estimate that using this single stellar evolution model for a $12 M_{\odot}$ star like Betelgeuse will result in a systematic uncertainty. Due to the stiff dependence on the core temperature, typical uncertainties on stellar profiles may lead to uncertainties which can be maximally estimated within ~ 1 order

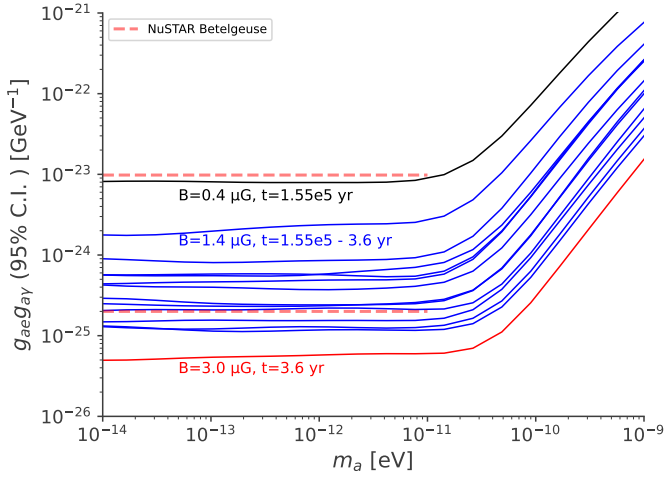


Fig. 6: The 95% C.I. upper limits of $g_{ae} \times g_{\gamma}$ as a function of ALP mass for Betelgeuse in the energy range 20 – 600 keV. The solid blue lines show the upper limit for each stellar model, assuming a representative value of $B_T = 1.4 \mu\text{G}$ with the top blue line corresponding to $t_{cc} = 1.55 \times 10^5$ yr and the bottom blue line corresponding to $t_{cc} = 3.6$ yr. The constraints will scale with different B_T as in Eq. 4, the solid black line shows the upper limit for the most conservative ($B_T = 0.4 \mu\text{G}$ and $t_{cc} = 1.55 \times 10^5$ yrs) and the solid red line for the most optimistic case ($B_T = 3.0 \mu\text{G}$ and $t_{cc} = 3.6$ yrs). For comparison, we also show the 95% C.I. upper limits of $g_{ae} \times g_{\gamma}$ obtained from Xiao et al. (2022) for the most conservative and optimistic cases with dashed red lines.

of magnitude of difference in the fluxes, leading to uncertainties within a factor $\sim 2 - 3$ on the resulting limits. This same mass assumption and uncertainty is negligible compared to the uncertainties on the time to core-collapse or the magnetic field on the line-of-sight between the detector and the respective star. Additionally, some regions in the sky are observed more often than others, giving us better statistics for the respective sources such as for the sources in the Cygnus region. Nevertheless, as reported by Xiao et al. (2022), their analysis can be extended essentially unchanged to other close-by supergiant stars strengthening the credibility of this analysis.

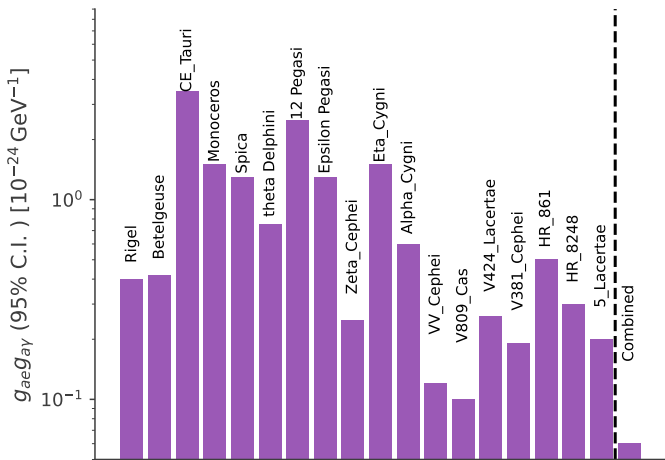


Fig. 7: The 95% C.I. upper limits of $g_{ae} \times g_{\gamma}$ for the entire star sample (individual stars and from a combined analysis) for $B_T = 1.4 \mu\text{G}$ and $t_{cc} = 6900$ yrs and $m_a < 10^{-11}$ eV.

Fig. 8 shows the 95% C.I. obtained from a combined analysis of all 18 stars for all stellar models ($t_{cc} = 1.55 \times 10^5 - 3.6$ yr) for the energy range 20 – 600 keV (extension to higher energies is shown in the Appendix A). We find the combined coupling range to be $g_{\gamma} \times g_{ae} = (0.008 - 2) \times 10^{-24} \text{ GeV}^{-1}$. This result improves the previous estimation by ~ 1 order of magnitude for the most conservative stellar model ($t_{cc} = 1.55 \times 10^5$ yr, $B_T = 0.4 \mu\text{G}$) and about a factor of 25 for the most optimistic (but unrealistic, see next section) case ($t_{cc} = 3.6$ yr, $B_T = 3.0 \mu\text{G}$). We also place limits on the ALP-photon coupling, g_{γ} , by assuming Primakoff emission as the only viable production channel and in which the ALP-electron coupling is switched off. We find the 95% C.I. on g_{γ} to be in the range $(0.13 - 1.26) \times 10^{-11} \text{ GeV}^{-1}$ depending on the magnetic field model and the time to core-collapse. This is a small improvement on the previous limits by Xiao et al. (2021) which sets the 95% C.I. on the ALP-photon coupling of $g_{\gamma} < (0.5 - 1.8) \times 10^{-11} \text{ GeV}^{-1}$.

The range of parameters obtained from this study of multiple stars with SPI also improves on estimations from previous studies performed with different instruments and alternative candidate sources (e.g., Barth et al. 2013; Dessert et al. 2019; Abeln et al. 2021a; Dessert et al. 2022, and references therein). This comparison is shown in Fig. 9. Ning & Safdi (2025) sets stronger constraints on the coupling product than our analysis, however the limitation of their study is discussed in the conclusion (Sec. 6).

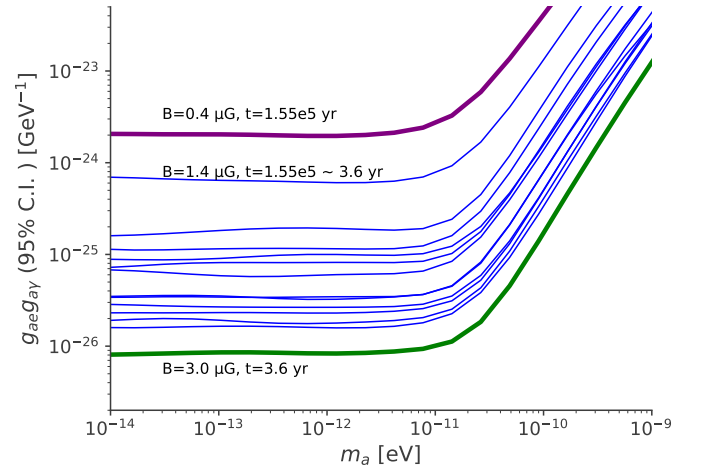


Fig. 8: The 95% C.I. upper limits of $g_{ae} \times g_{\gamma}$ as a function of ALP mass m_a for the combined analysis of all 18 stars for the energy range 20 – 600 keV. The solid blue lines show the upper limit for each stellar model, assuming a representative value of $B_T = 1.4 \mu\text{G}$ with the top blue line corresponding to $t_{cc} = 1.55 \times 10^5$ yr and the bottom blue line corresponding to $t_{cc} = 3.6$ yr. The solid purple line shows the upper limit for the most conservative ($B_T = 0.4 \mu\text{G}$ and $t_{cc} = 1.55 \times 10^5$ yr) and the solid green line for the most optimistic case ($B_T = 3.0 \mu\text{G}$ and $t_{cc} = 3.6$ yr).

5.2. Conservative results

To obtain more conservative and realistic constraints on ALP couplings, we consider a scenario in which all but one star in our sample is assumed to be in an early stage of stellar evolution. This is specifically the early Helium burning phase corresponding to $t_{cc} = 1.55 \times 10^5$ yr. One star at a time is then placed in a more advanced phase with time to core-collapse of $t_{cc} = 2.3 \times 10^4$ yr, representing a later stage of Helium burning. For this conserva-

Common Name	Gal. long	Gal. lat	Distance [kpc]	Mass [M_{\odot}]	$g_{ae} \times g_{a\gamma}$	$g_{a\gamma}$	511 keV	1.8 MeV	M_{Al} [M_{\odot}]
	[deg]	[deg]			2σ UL	2σ UL	3σ UL	3σ UL	3σ UL
Spica	316.11	50.84	0.077 ± 0.004	$11.43^{+1.15}_{-1.15}$	27.7	4.36	35.6	11.8	6
ϵ Pegasi	65.57	-31.45	0.211 ± 0.006	$11.7^{+0.8}_{-0.8}$	13.5	3.26	30.3	9.7	37
Betelgeuse	199.78	-8.95	0.222 ± 0.040	$11.6^{+5.0}_{-3.9}$	8.1	2.15	11.1	4.4	19
ζ Cephei	103.06	1.66	0.256 ± 0.006	$10.1^{+0.1}_{-0.1}$	3.3	1.97	1.1	0.4	2
Rigel	209.24	-25.24	0.264 ± 0.024	$21.0^{+3.0}_{-3.0}$	11.7	3.31	5.7	1.8	11
ξ Cygni	71.01	3.36	0.278 ± 0.029	8.0	25.1	5.69	13.4	4.6	30
S Monocerotis A	202.93	2.19	0.282 ± 0.040	29.1	41.8	5.51	45.9	13.3	90
CE Tauri	187.17	-8.07	0.326 ± 0.070	$14.37^{+2.00}_{-2.00}$	50.8	5.86	289.0	41.4	375
12 Pegasi	76.64	-22.82	0.415 ± 0.031	$6.3^{+0.7}_{-0.7}$	56.4	6.68	100.0	17.0	250
5 Lacertae	99.66	-8.65	0.505 ± 0.046	$5.11^{+0.18}_{-0.18}$	17.2	3.60	1.9	0.7	15
VV Cephei	104.92	7.04	0.599 ± 0.083	$10.6^{+1.0}_{-1.0}$	4.7	3.11	1.1	0.4	13
θ Delphini	57.94	-16.60	0.629 ± 0.029	$5.60^{+3.0}_{-3.0}$	22.5	4.98	45.8	14.9	503
V381 Cephei	98.18	6.35	0.631 ± 0.086	12.0	5.1	2.01	2.3	0.9	31
V424 Lacertae	104.58	-8.99	0.634 ± 0.075	$6.8^{+1.0}_{-1.0}$	4.2	4.93	1.2	0.5	16
HR 861	135.95	4.66	0.639 ± 0.039	$9.2^{+0.5}_{-0.5}$	14.4	2.30	1.9	0.7	25
V809 Cassiopeia	112.61	1.72	0.730 ± 0.074	$8.3^{+0.5}_{-0.5}$	2.0	1.19	0.7	0.3	13
HR 8248	90.83	-4.30	0.746 ± 0.039	$6.3^{+0.7}_{-0.7}$	4.6	1.66	4.7	1.8	85
α Cygni	84.28	1.99	0.802 ± 0.066	$19.0^{+4.0}_{-4.0}$	11.5	3.58	11.5	3.9	213
combined:					1.9	1.26			

Table 1: List of massive stars used in this analysis along with their Galactic coordinates, distance and mass (obtained from Mukhopadhyay et al. (2020)). We also show the most conservative ($B_T = 0.4 \mu\text{G}$, $t_{\text{cc}} = 1.55 \times 10^5 \text{ yr}$) 95% confidence interval upper limit obtained for the coupling product $g_{ae} \times g_{a\gamma}$ and for the photon only coupling $g_{a\gamma}$. In addition, the 3σ flux upper limits for the 511 keV and the 1809 keV are also listed. Finally, the ^{26}Al mass expected based on the 1809 keV flux is also shown. The units of $g_{ae} \times g_{a\gamma}$, $g_{a\gamma}$, the line fluxes, and the ^{26}Al masses are $10^{-24} \text{ GeV}^{-1}$, $10^{-11} \text{ GeV}^{-1}$, $10^{-5} \text{ ph cm}^{-2} \text{ s}^{-1}$, and $10^{-5} M_{\odot}$, respectively.

tive scenario, we assume a uniform Galactic magnetic field of $B_T = 0.4 \mu\text{G}$. This approach avoids the overly optimistic assumption that all stars are simultaneously near core collapse and allows us to explore the effect of evolutionary differences on the derived limits.

By iteratively assigning the more advanced stage to each of the 18 stars, while keeping the others in the early phase, we obtain a range of constraints that reflect the potential diversity in the actual stellar states. This method also mitigates the variability seen in individual star constraints (as illustrated in Fig. 7), providing a more balanced estimate of the overall sensitivity. Fig. 10 shows the resulting range of 95% C.I upper limits on the product $g_{a\gamma} \times g_{ae} = (0.27 - 1.25) \times 10^{-24} \text{ GeV}^{-1}$. The strongest constraint is obtained when V809 Cassiopeia is placed in the advanced stage ($t_{\text{cc}} = 2.3 \times 10^4 \text{ yr}$), while the weakest arises when CE Tauri is assumed to be the star closer to collapse. This outcome is consistent with the individual star sensitivities shown earlier and emphasizes how the depth of observation in each region influences the results. This conservative framework provides a more robust and physically motivated estimate of the ALP parameter space, accounting for astrophysical uncertainties in stellar evolution stages.

5.3. Gamma-ray lines

While the focus of this work is to search for ALPs, we also investigate the possibility of these red super giants to show significant γ -ray line emission at 511 keV (positron annihilation) and 1809 keV (decay of radioactive ^{26}Al). Typically, we find limits on the lines on the order of $10^{-4} \text{ ph cm}^{-2} \text{ s}^{-1}$ at 511 keV and $10^{-5} \text{ ph cm}^{-2} \text{ s}^{-1}$ at 1809 keV, with V809 Cassiopeia to have the strongest constraints in terms of flux. Tab. 1 shows the 3σ upper-limits for the 511 keV and 1809 keV flux for all the stars. As for the most interesting candidate to search for the 1809 keV line, γ^2 Velorum (Oberlack et al. 1996; Pleintinger 2020), any red super giant might be of interest as massive star winds would eject ^{26}Al . The mass yield is calculated as follows:

$$M_{\text{Al}} = 4\pi d^2 \times F_{\text{Al}} \times m_{\text{Al}} \times \tau_{\text{Al}}, \quad (9)$$

where, d is the distance to the star, F_{Al} is the expected ^{26}Al flux, $m_{\text{Al}} = 26 \text{ g/mol}$ is the atomic mass of ^{26}Al , and $\tau_{\text{Al}} = 1.04 \text{ Myr}$ is the lifetime of ^{26}Al . The respective ^{26}Al mass yield expected from each star based on the 1809 keV flux upper limit is also listed in Tab. 1. For the closest star in our sample, Spica, with a distance of 77 pc and a mass of $\sim 12 M_{\odot}$, we find an upper limit on the 1809 keV line flux of $1.2 \times 10^{-4} \text{ ph cm}^{-2} \text{ s}^{-1}$, which would correspond to an instantaneous ^{26}Al mass of $6 \times 10^{-5} M_{\odot}$. This is more

than two orders of magnitude above the expectations from massive star evolution models (e.g., Ekström et al. 2012; Limongi & Chieffi 2018). As for the most massive stars in our sample, Rigel ($\sim 21 M_{\odot}$) and Monoceros A ($\sim 29.1 M_{\odot}$), the upper limit on the ^{26}Al mass is around $1.1 \times 10^{-4} M_{\odot}$ and $9.0 \times 10^{-4} M_{\odot}$. Wind yields of red super giants in the mass range of 20–30 M_{\odot} would be found around 5×10^{-7} – $5 \times 10^{-5} M_{\odot}$, so that current MeV observations are approaching the interesting region of massive star evolution models.

For the 511 keV line in the case of Betelgeuse, we found the energy bin from 508–514 keV is not consistent with zero. We attribute this to an incomplete modelling of the diffuse emission with the smooth description from Siegert et al. (2016). In addition, individual sources with such a strong 511 keV line may be unphysical as their only source would be ^{26}Al for which we would explain about 41% of the 1809 keV line flux at 511 keV.

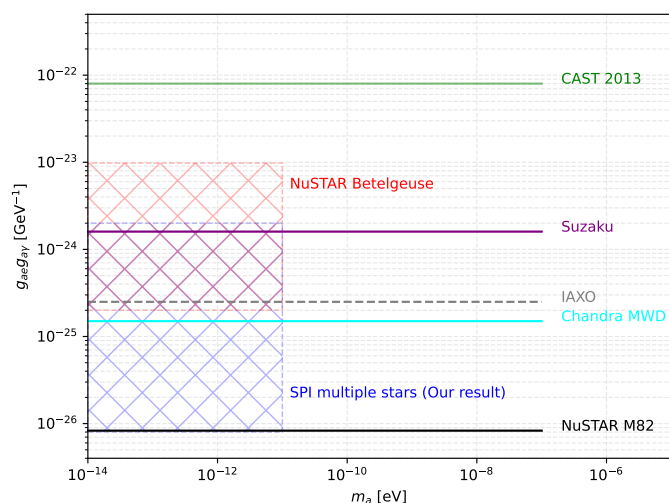


Fig. 9: Comparison of $g_{ae} \times g_{\gamma}$ across different instruments and different astrophysical objects. The bounds for CAST are obtained from Barth et al. (2013), NuSTAR’s Betelgeuse bounds from Xiao et al. (2022), Suzaku bounds from Dessert et al. (2019), projected sensitivity of IAXO from Abeln et al. (2021a), Chandra’s MWD study from Dessert et al. (2022), and NuSTAR’s M82 bounds from Ning & Safdi (2025). This study improves the previous limits by over an order of magnitude for the most optimistic case. The study of M82 with NuSTAR might still provide the tightest constraints in the literature, however the limitation of their analysis is discussed in the conclusion.

6. Conclusion and outlook

In this work, we present new constraints on ALPs coupled to both electrons and photons, using 22 years of INTEGRAL/SPI observations of 18 nearby red super giants. The hot dense stellar interiors provide perfect conditions for the production of ALPs through Compton, Primakoff and to a lesser extent bremsstrahlung processes, which are transformed back to photons in the Galactic magnetic field in the direction towards the star. Extending previous studies that focused on the hard X-ray emission from the direction of Betelgeuse, we perform a combined γ -ray analysis in the 20 – 2000 keV range across a diverse sample of evolved massive stars. We compiled individual limits from a set of 18 red super giants and conducted a Bayesian hierarchical model to constrain the ALP couplings in a joint fit. We find no signif-

icant ALP-induced emission from any individual source. This allows us to set stringent 95% C.I upper limits on the product $g_{\gamma} \times g_{ae}$ as a function of ALP mass m_a . The best case constraints from our full sample analysis improve upon previous limits by up to a factor of ~ 25 , and reach sensitivity down to $g_{\gamma} \times g_{ae} = 8 \times 10^{-27} \text{ GeV}^{-1}$ for ultra-light ALPs with $m_a \leq 10^{-11} \text{ eV}$. We also explore a conservative scenario accounting for uncertainties in stellar evolutionary stages, assigning one star at a time to a more advanced burning phase while keeping others in earlier phases. This yields a robust constraint range of $g_{\gamma} \times g_{ae} = (0.27\text{--}1.25) \times 10^{-24} \text{ GeV}^{-1}$. Finally, we also look at a Primakoff only emission scenario and constrain the ALP-photon coupling to be in the range $g_{\gamma} = (0.13\text{--}1.26) \times 10^{-11} \text{ GeV}^{-1}$.

Our constraints are $\sim 2\text{--}3$ orders of magnitude better than the bounds obtained from CAST for Solar ALPs (e.g., Barth et al. 2013). Furthermore, we also improve on the limits predicted by *Chandra*’s study of conversion in magnetic white dwarfs (e.g., Dessert et al. 2022). Our results provide one of the most stringent limits to date on ALP couplings in this mass range using γ -ray data from evolved stars. Without modelling the intrinsic astrophysical emission mechanisms in entire galaxies (Ning & Safdi 2025), estimating ALPs only contribution might be misleading, and could result in overly optimistic limits. This was shown in contemporary work about diffuse emission from dark matter in the Milky Way Berteaud et al. (2022); Siegert et al. (2024, 2022); Calore et al. (2023). Future improvements may come from more detailed stellar modelling, better understanding of Galactic magnetic field structures, and next-generation γ -ray instruments with improved sensitivity and resolution, such as NASA’s Compton Spectrometer and Imager (COSI) Small Explorer mission which will be launched in 2027 (Tomsick et al. 2019, 2021). This work demonstrates the power of multi-source analyses in probing the ALP parameter space and contributes a significant step forward in the search for new physics beyond the Standard Model.

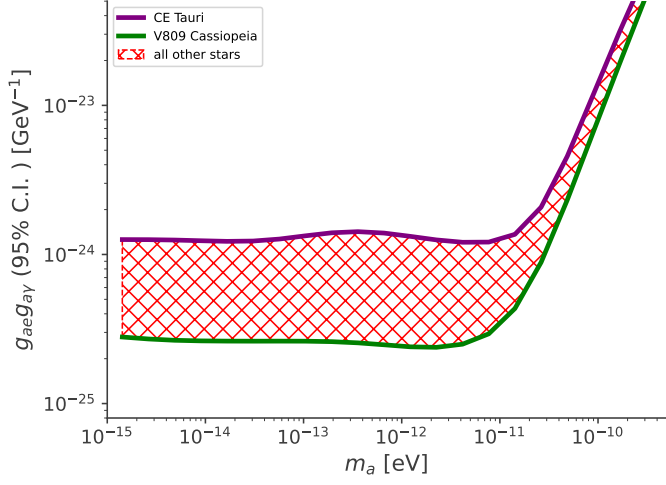


Fig. 10: Range of 95% C.I. upper limits on $g_{a\gamma} \times g_{ae}$ as a function of ALP mass m_a , derived from the conservative scenario in which one star out of 18 is assumed to be in a later evolutionary stage ($t_{cc} = 2.3 \times 10^4$ yr), while the remaining 17 stars are fixed at an earlier He-burning phase ($t_{cc} = 1.55 \times 10^5$ yr) and a uniform $B_T = 0.4 \mu\text{G}$. The strongest constraint is obtained when V809 Cassiopeia is assumed to be closer to core collapse (green), and the weakest when CE Tauri is (purple). The hatched region is the range of constraints obtained when every other star is individually placed in the more advanced He-burning phase. This method accounts for uncertainties in stellar evolution and provides a realistic range of possible limits.

Appendix A: Extended energy range

Fig. A.1 shows the 95% C.I. for an extended energy range of 20–2000 keV of three different stellar models as quoted. The limits obtained for this extended energy range are essentially identical to those obtained for the energy range 20 – 600 keV. This is expected as the ALP spectrum peaks around/below 550 keV depending on the stellar model, and thus higher energies do not significantly affect the ALP constraints.

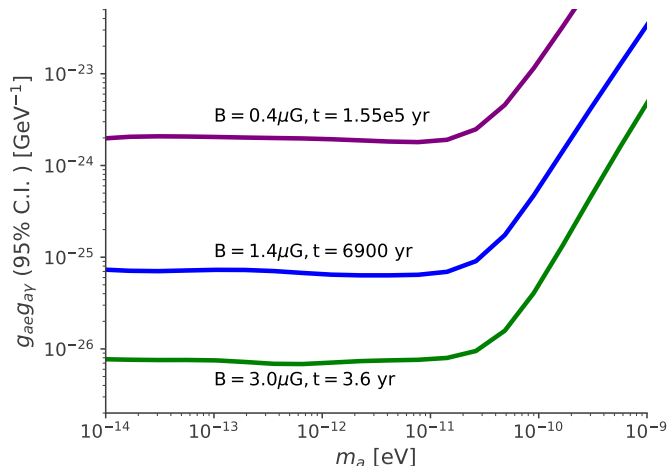


Fig. A.1: The 95% C.I. upper limits of $g_{ae} \times g_{\gamma}$ as a function of ALP mass m_a for the combined analysis of all 18 stars for the energy range 20 – 2000 keV. The solid blue line shows the upper limit for $t_{cc} = 6900$ yr, assuming a representative value of $B_T = 1.4 \mu\text{G}$. The solid purple line shows the upper limit for the most conservative ($B_T = 0.4 \mu\text{G}$ and $t_{cc} = 1.55 \times 10^5$ yr) and the green line for the most optimistic case ($B_T = 3.0 \mu\text{G}$ and $t_{cc} = 3.6$ yr). Note that the limits for the extended energy range are identical to the ones shown in Fig. 8 as the ALP spectrum peaks around 500 keV or below.

Acknowledgements. Saurabh Mittal acknowledges support by the Bundesministerium für Wirtschaft und Energie via the Deutsches Zentrum für Luft- und Raumfahrt (DLR) under Contract No. 50 OO 2219. Laura Eisenberger acknowledges support by the Bundesministerium für Wirtschaft und Energie via the Deutsches Zentrum für Luft- und Raumfahrt (DLR) under Contract No. 50 OR 2413 and is grateful for the support of the Studienstiftung des Deutschen Volkes. Dimitris Tsatsis acknowledges support from the DFG/LIS project SI 2502/6-1, project number 551127478. This article is based on work from COST Action COSMIC WISPerS CA21106, supported by COST (European Cooperation in Science and Technology). The work of AM and AL was partially supported by the research grant number 2022E2J4RK “PANTHEON: Perspectives in Astroparticle and Neutrino THEory with Old and New messengers” under the program PRIN 2022 (Mission 4, Component 1, CUP I53D23001110006) funded by the Italian Ministero dell’Università e della Ricerca (MUR) and by the European Union – Next Generation EU. This work is (partially) supported by ICSC – Centro Nazionale di Ricerca in High Performance Computing, Big Data and Quantum Computing, funded by European Union–NextGenerationEU. PC is supported by the Swedish Research Council under contract 2022-04283.

References

Abbott, L. F. & Sikivie, P. 1983, *Phys. Lett. B*, 120, 133
 Abeln, A., Altenmüller, K., Arguedas Cuendis, S., et al. 2021a, *Journal of High Energy Physics*, 2021, 1
 Abeln, A. et al. 2021b, *JHEP*, 05, 137
 Adams, C. B. et al. 2022, in *Snowmass 2021*
 Agrawal, P. et al. 2021, *Eur. Phys. J. C*, 81, 1015
 Ahyoune, S. et al. 2025, *JHEP*, 02, 159
 Altenmüller, K. et al. 2024, *Phys. Rev. Lett.*, 133, 221005

Andriamonje, S. et al. 2007, *JCAP*, 04, 010
 Antel, C. et al. 2023, *Eur. Phys. J. C*, 83, 1122
 Arcusa, A. et al. 2025 [arXiv:2504.00079]
 Arias, P., Cadamuro, D., Goodsell, M., et al. 2012, *JCAP*, 06, 013
 Armengaud, E. et al. 2019, *JCAP*, 06, 047
 Arvanitaki, A., Dimopoulos, S., Dubovsky, S., Kaloper, N., & March-Russell, J. 2010, *Phys. Rev. D*, 81, 123530
 Ayala, A., Domínguez, I., Giannotti, M., Mirizzi, A., & Straniero, O. 2014, *Physical review letters*, 113, 191302
 Barth, K., Belov, A., Beltran, B., et al. 2013, *Journal of cosmology and astroparticle physics*, 2013, 010
 Berteaud, J., Calore, F., Iguaz, J., Serpico, P. D., & Siegert, T. 2022, arXiv.org, arXiv:2202.07483
 Bertolami, M. M., Melendez, B. E., Althaus, L. G., & Isern, J. 2014, *Journal of Cosmology and Astroparticle Physics*, 2014, 069
 Bouchet, L., Jourdain, E., Roques, J.-P., et al. 2008, *The Astrophysical Journal*, 679, 1315
 Brockway, J. W., Carlson, E. D., & Raffelt, G. G. 1996, *Phys. Lett. B*, 383, 439
 Calore, F., Dekker, A., Serpico, P. D., & Siegert, T. 2023, *Monthly Notices of the Royal Astronomical Society*, 520, 4167
 Capozzi, F. & Raffelt, G. 2020, *Physical Review D*, 102, 083007
 Carena, P., Giannotti, M., Isern, J., Mirizzi, A., & Straniero, O. 2025, *Phys. Rept.*, 1117, 1
 Carlson, E. D. 1995, *Physics Letters B*, 344, 245
 Cetin, S. A. 2024, *PoS. COSMICWISPerS*, 030
 Cicoli, M., Conlon, J. P., Maharana, A., et al. 2024, *Phys. Rept.*, 1059, 1
 Cicoli, M., Goodsell, M., & Ringwald, A. 2012, *JHEP*, 10, 146
 Courvoisier, T. J. L., Walter, R., Beckmann, V., et al. 2003, 411, L53
 Dessert, C., Long, A. J., & Safdi, B. R. 2019, *Physical review letters*, 123, 061104
 Dessert, C., Long, A. J., & Safdi, B. R. 2022, *Physical Review Letters*, 128, 071102
 Di Luzio, L., Giannotti, M., Nardi, E., & Visinelli, L. 2020, *Physics Reports*, 870, 1
 Diehl, R., Siegert, T., Greiner, J., et al. 2018, *Astronomy & Astrophysics*, 611, A12
 Dine, M. & Fischler, W. 1983, *Phys. Lett. B*, 120, 137
 Dolan, M. J., Hiskens, F. J., & Volkas, R. R. 2022, *Journal of Cosmology and Astroparticle Physics*, 2022, 096
 Dolan, M. M., Mathews, G. J., Lam, D. D., et al. 2016, *The Astrophysical Journal*, 819, 7
 Ekström, S., Georgy, C., Eggenberger, P., et al. 2012, *A&A*, 537, A146
 Galanti, G., Nava, L., Roncadelli, M., Tavecchio, F., & Bonnoli, G. 2023, *Phys. Rev. Lett.*, 131, 251001
 Giannotti, M. 2023, *J. Phys. Conf. Ser.*, 2502, 012003
 Giannotti, M., Irastorza, I., Redondo, J., & Ringwald, A. 2016, *JCAP*, 05, 057
 Giannotti, M., Irastorza, I. G., Redondo, J., Ringwald, A., & Saikawa, K. 2017, *Journal of Cosmology and Astroparticle Physics*, 2017, 010
 Grifols, J. A., Masso, E., & Toldra, R. 1996, *Phys. Rev. Lett.*, 77, 2372
 Harrison, F. A. et al. 2013, *Astrophys. J.*, 770, 103
 Hoof, S. & Schulz, L. 2023, *JCAP*, 03, 054
 Jaeckel, J. & Ringwald, A. 2010, *Ann. Rev. Nucl. Part. Sci.*, 60, 405
 Lella, A., Calore, F., Carena, P., et al. 2024, *JCAP*, 11, 009
 Limongi, M. & Chieffi, A. 2018, *ApJS*, 237, 13
 Mukhopadhyay, M., Lunardini, C., Timmes, F., & Zuber, K. 2020, *The Astrophysical Journal*, 899, 153
 Ning, O. & Safdi, B. R. 2025 [arXiv:2503.09682]
 Oberlack, U., Bennett, K., Bloemen, H., et al. 1996, *Astronomy and Astrophysics Supplement*, 120, 311
 Payez, A., Evoli, C., Fischer, T., et al. 2015, *JCAP*, 02, 006
 Peccei, R. D. & Quinn, H. R. 1977a, *Phys. Rev. D*, 16, 1791
 Peccei, R. D. & Quinn, H. R. 1977b, *Phys. Rev. Lett.*, 38, 1440
 Pleintinger, M. M. M. 2020, PhD Dissertation
 Preskill, J., Wise, M. B., & Wilczek, F. 1983, *Phys. Lett. B*, 120, 127
 Primakoff, H. 1951, *Physical Review*, 81, 899
 Raffelt, G. G. 1996, *Stars as laboratories for fundamental physics: The astrophysics of neutrinos, axions, and other weakly interacting particles*
 Raffelt, G. G. 1999, *Ann. Rev. Nucl. Part. Sci.*, 49, 163
 Ringwald, A. 2014, *Axions and Axion-Like Particles*
 Siegert, T., Berteaud, J., Calore, F., Serpico, P. D., & Weinberger, C. 2022, arXiv.org, arXiv:2202.04574
 Siegert, T., Calore, F., & Serpico, P. D. 2024, *Monthly Notices of the Royal Astronomical Society*, 528, 3433
 Siegert, T., Diehl, R., Khachatryan, G., et al. 2016, *Astronomy & Astrophysics*, 586, A84
 Siegert, T., Diehl, R., Weinberger, C., et al. 2019, *Astronomy & Astrophysics*, 626, A73
 Sikivie, P. 1983, *Phys. Rev. Lett.*, 51, 1415, [Erratum: *Phys.Rev.Lett.* 52, 695 (1984)]

- Straniero, O., Ayala, A., Giannotti, M., et al. 2015, in 11th Patras Workshop on Axions, WIMPs and WISPs No. PUBDB-2017-00134, Verlag Deutsches Elektronen-Synchrotron
- Straniero, O., Dominguez, I., Piersanti, L., Giannotti, M., & Mirizzi, A. 2019, *The Astrophysical Journal*, 881, 158
- Straniero, O., Pallanca, C., Dalessandro, E., et al. 2020, *Astronomy & Astrophysics*, 644, A166
- Strong, A. W., Diehl, R., Haloin, H., et al. 2005, *Astronomy & Astrophysics*, 444, 495
- Tomsick, J., Boggs, S., Zoglauer, A., et al. 2021, in American Astronomical Society Meeting Abstracts, Vol. 53, American Astronomical Society Meeting Abstracts, 315.01
- Tomsick, J. A., Zoglauer, A., Sleator, C., et al. 2019, arXiv.org, arXiv:1908.04334
- van Bibber, K., McIntyre, P. M., Morris, D. E., & Raffelt, G. G. 1989, *Phys. Rev. D*, 39, 2089
- Vedrenne, G., Roques, J.-P., Schönfelder, V., et al. 2003, *Astronomy & Astrophysics*, 411, L63
- Vianello, G., Lauer, R. J., Younk, P., et al. 2015, arXiv preprint arXiv:1507.08343
- Weinberg, S. 1978, *Phys. Rev. Lett.*, 40, 223
- Wilczek, F. 1978, *Phys. Rev. Lett.*, 40, 279
- Winkler, C., Di Cocco, G., Gehrels, N., et al. 2003, *Astronomy & Astrophysics*, 411, L1
- Xiao, M., Carena, P., Giannotti, M., et al. 2022, *Physical Review D*, 106, 123019
- Xiao, M., Perez, K. M., Giannotti, M., et al. 2021, *Phys. Rev. Lett.*, 126, 031101